ELSEVIER

Journal of Structural Geology 26 (2004) 1897–1911

JOURNAL OF STRUCTURAL GEOLOGY

www.elsevier.com/locate/jsg

Three-dimensional distinct element modelling of relay growth and breaching along normal faults

J. Imber[a,1], G.W. Tuckwell[b,2], C. Childs[a,*], J.J. Walsh[a], T. Manzocchi[a], A.E. Heath[c], C.G. Bonson[a], J. Strand[a]

[a]*Fault Analysis Group, Department of Geology, University College Dublin, Belfield, Dublin 4, Ireland*
[b]*School of Earth Sciences and Geography, Keele University, Keele, Staffordshire ST5 5BG, UK*
[c]*Fault Analysis Group, Department of Earth Sciences, University of Liverpool, Liverpool L69 3GP, UK*

Received 24 January 2003; received in revised form 4 February 2004; accepted 26 February 2004

Available online 14 May 2004

Abstract

Three-dimensional numerical models of neutral (i.e. slip-parallel) relay zones on normal faults that cut massive sandstone host rocks have been constructed using the distinct element method code, Particle Flow Code in 3-D (PFC^{3D}). The models successfully reproduce the geometries, displacement profiles and strains observed in natural relay zones. In contrast to boundary element method simulations, the modelled relay ramps dip towards the hanging wall, consistent with observations of most natural relay zones. The modelling shows that relay zones are stable structures that 'grow' by progressive rotation of an approximately planar relay ramp without significant propagation of the relay-bounding faults prior to breaching. Stable growth is terminated when a breaching fault propagates across the top or bottom of the relay ramp. Breaching fault propagation is not instantaneous and the ramp continues to rotate, and therefore transfer displacement between the relay-bounding faults, until they become fully hard linked. Following hard linkage, displacement is accommodated by slip on the through-going fault surface. The modelling results confirm previous conceptual models of relay growth and breaching based on geometric and kinematic analysis of natural relay zones.

Keywords: Faults; Segmentation; Linkage; Relays; Numerical modelling

1. Introduction

Displacements on normal faults are rarely accommodated on a single well-defined slip surface, but are partitioned between interacting fault segments (Walsh and Watterson, 1990, 1991; Peacock and Sanderson, 1991, 1994; Cartwright et al., 1995, 1996; Childs et al., 1995, 1996; Willemse, 1997). Fault segmentation occurs across a wide range of length scales (Stewart and Hancock, 1991; Trudgill and Cartwright, 1994; Walsh et al., 2003).

The transfer of displacement from one fault segment to another segment that dips in the same direction most often occurs through relay structures (Chadwick, 1986; Ramsay and Huber, 1987; Larsen, 1988), which are zones of high fault-parallel shear strain that provide soft linkage (Walsh and Watterson, 1991) between two interacting fault segments (Fig. 1a–c). Breaching occurs when the fault segments are replaced by a single, through-going fault surface. Typically, breaching faults propagate across either the top or bottom of the relay ramp (e.g. Peacock and Sanderson, 1991, 1994; Childs et al., 1995; Fig. 1a and d) though, in previously jointed rocks, breaching faults may reactivate pre-existing joint sets to cut across the centre of the relay zone (Peacock, 2001). Intact relay zones are suggested to be important sediment entry points into fault-bounded extensional basins (Gawthorpe and Leeder, 2000), and both intact and breached relays can influence the sealing capacities and/or flow properties of faults in hydrocarbon reservoirs (Morley et al., 1990; Childs et al., 1995). Thus, knowledge of relay growth and breaching is important to understand the kinematics of fault growth and segment

* Corresponding author. Tel.: +353-1-716-2606; fax: +353-1-716-2607.
E-mail address: fault@fag.ucd.ie (C. Childs).
[1] Present address: Reactivation Research Group, Department of Earth Sciences, University of Durham, Science Laboratories, South Road, Durham DH1 3LE, UK
[2] Present address: STATS Geophysical, Porterswood House, Porterswood, St. Albans, AL3 6PQ, UK

0191-8141/$ - see front matter © 2004 Elsevier Ltd. All rights reserved.
doi:10.1016/j.jsg.2004.02.010

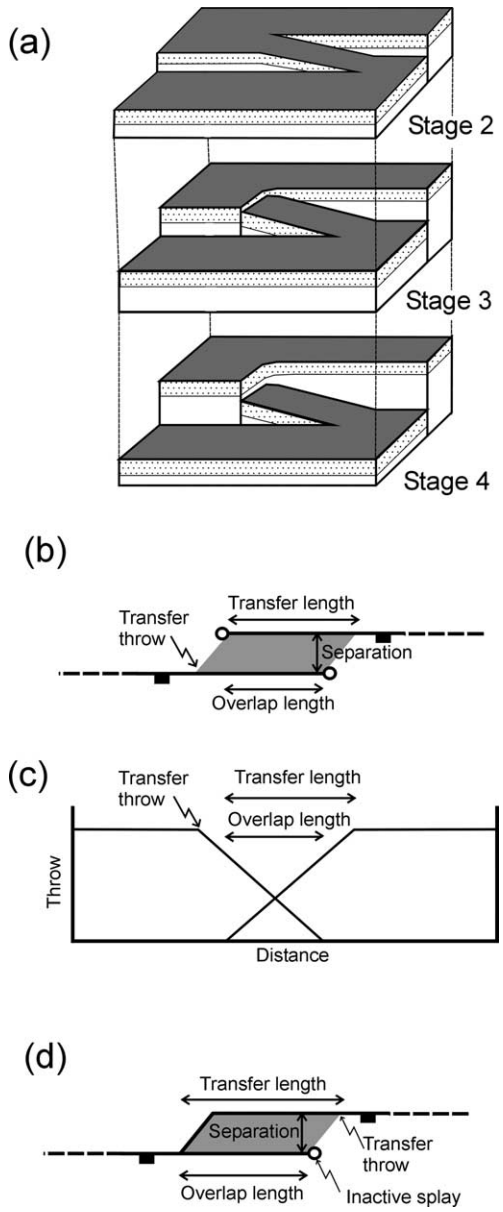

Fig. 1. (a) Schematic block diagram showing the stages of relay growth and breaching inferred from geometric analysis of outcrop-scale, neutral relay zones, i.e. relay zones in which the fault slip vector is parallel to the local tips of the overlapping faults (adapted from Peacock and Sanderson, 1994). Stage 1, which is when the fault segments are isolated and non-interacting, is not always required (Walsh et al., 2003) and is not shown here; Stage 2 is when the fault segments interact and a relay ramp develops; Stage 3 is when a breaching fault propagates across the base or, as shown here, the top of the relay ramp; Stage 4 is when the fault segments are fully hard linked. Peacock and Sanderson (1994) have pointed out that different levels within the same relay zone may have different displacements and hence be at different stages of development. (b) Schematic map showing the nomenclature for an intact relay zone. (c) Schematic fault throw vs. distance graph for the relay zone shown in (b). 'Transfer length' is the distance between the fault tip and the point at which the throw (or displacement) gradient starts to increase towards the relay zone. 'Transfer throw' is the fault throw at the point at which the throw (or displacement) gradient starts to increase towards the relay zone. Relay strain = transfer throw/transfer length; relay shape = transfer length/overlap length. (d) Schematic map showing the nomenclature for a breached relay zone.

linkage, fault zone development (Cartwright et al., 1995; Walsh et al., 2003) and has direct relevance to hydrocarbon exploration and production (Peacock, 2002).

Conceptual models of relay growth and breaching are most often based on detailed geometric analyses of outcrop- to seismic-scale relays (Peacock and Sanderson, 1991, 1994; Trudgill and Cartwright, 1994; Childs et al., 1995; Huggins et al., 1995; Cartwright et al., 1996; Walsh et al., 1999). These models suggest that breaching occurs when strain can no longer be accommodated by continuous deformation within the relay zone (e.g. Fig. 1a). There are, however, few published kinematic (as opposed to purely geometric) studies of natural relays that provide direct observational support for such conceptual models. A notable exception is the work of Childs et al. (1993, 1995) who examined the growth and breaching of relay zones on syn-sedimentary normal faults from 3-D seismic datasets and analogue models. These authors applied displacement backstripping methods (Chapman and Meneilly, 1991; Petersen et al., 1992; Childs et al., 1993; Clausen and Korstgård, 1994) to reconstruct the pre-breaching fault displacements and relay ramp geometries. These kinematic studies support the simple geometric models in which relays are established, maintain a stable configuration and then eventually breach. The conditions required for accurate application of the displacement backstripping method (Childs et al., 1993, 1995) are rarely met and, even where they are, the lateral resolution of many seismic datasets does not permit kinematic analysis of relay zones where the fault separation is less than a few tens of metres. Similarly, the imperfect (i.e. $<$3-D) exposure of relays in outcrop and the absence of growth strata in most cases preclude kinematic analysis. Numerical models that capture the mechanics of fault segment interaction therefore provide a useful tool to examine growth and breaching of sub-seismic relays.

The aims of this study are twofold. The first is to show that three-dimensional (3-D) numerical simulations based on the distinct element method (DEM; Cundall and Strack, 1979) can be used to model the kinematics of a small, neutral (i.e. 'slip-parallel') relay zone (Peacock and Sanderson, 1991; Walsh et al., 1999; Fig. 1a) in a massive, intact sandstone from the time the overlapping faults first become geometrically coherent (i.e. conserving and transferring displacements between the segments; see Walsh and Watterson, 1991), to the point of relay breaching and beyond. The second aim is to understand better the stability and breaching of relay ramps. Crucially, the DEM as implemented in the program 'Particle Flow Code in 3-D' (PFC^{3D}; Itasca Consulting Group, 1999a) allows realistic modelling of fracture propagation and accumulation of large fault displacements and inelastic strains (e.g. Strayer and Suppe, 2002), difficult feats using continuum numerical schemes (Morgan and Boettcher, 1999). Our work therefore complements previous studies into the mechanics of fault segment interaction using boundary element method simulations based on the theory of linear elasticity (Section 2).

We should emphasize, however, that the question of how relay zones *initiate* was not addressed by our modelling. Relay zones can form through bifurcation of a propagating fault tip-line, propagation of a segmented fault array or through lateral propagation and subsequent interaction of previously independent structures (Mandl, 1987; Peacock and Sanderson, 1991, 1994; Childs et al., 1995, 1996; Huggins et al., 1995; Cartwright et al., 1996; see Walsh et al., 2003 for discussion). Though a distinction between these mechanisms is not always clear from natural data (Childs et al., 1995) our modelling results are believed to be valid for all neutral relay zones regardless of how they initiated.

2. Previous work

The boundary element method (BEM) treats a faulted rock volume as a homogeneous, linear elastic material cut by displacement discontinuities. Fault surfaces are discretized as arbitrarily shaped arrays of polygonal elements and the displacement is assumed to be constant across each element (e.g. Willemse, 1997; Crider and Pollard, 1998). In the boundary element method code 'Poly3d' (Thomas, 1993), the model is loaded by prescribing tractions or displacements at the centre of each element and/or applying a remote stress or strain at the model boundaries. The program calculates the slip on each element to determine the stress and strain fields in the rock volume surrounding the faults. Fault segments are therefore able to interact through their overlapping stress fields. A fundamental limitation of the boundary element method is that fault displacements are accommodated exclusively by elastic deformation in the surrounding rock volume. Thus, although the BEM captures the mechanics of an idealized, single slip event, it cannot be used to model actual fault propagation or stress relaxation during relay growth and breaching.

Willemse (1997) studied the influence of fault aspect ratio (i.e. fault strike dimension/fault dip dimension; Nicol et al., 1996), overlap length and separation (Fig. 1b) on fault segment interaction in a series of Poly3d models in which two blind, overlapping faults with elliptical tip-lines are embedded in an elastic whole space and dip at 60° towards their mutual hanging wall. The models suggest that the degree of interaction increases with increasing fault aspect ratio and overlap length and with decreasing fault separation. These results provide a mechanical rationale for the more frequent occurrence of overlapping relative to underlapping fault segments (Willemse et al., 1996; Willemse, 1997). Crider and Pollard (1998) used a BEM simulation to determine the Coulomb shear stress distribution in the volume surrounding two dipping fault segments with semi-circular tip-lines embedded in an elastic half space. They assumed that linkage is most likely to initiate in regions of increased Coulomb shear stress. The modelling shows that the magnitude of shear stress varies with fault dip dimensions and overlap length, and that the greatest stresses always occur where the fault tip-lines are closest, i.e. in the centre to upper relay ramp. Though Crider and Pollard's (1998) results are broadly consistent with previous conceptual models of relay growth and breaching (e.g. Peacock and Sanderson, 1991, 1994; Childs et al., 1993, 1995), the BEM simulations do not accurately reproduce the geometries of natural relay ramps and cannot model relay breaching: whereas most natural relay ramps have a component of dip *towards* the hanging wall fault (e.g. Huggins et al., 1995), the modelled ramps have a component of dip *away* from the hanging wall (Crider and Pollard, 1998, fig. 10; see also Peacock, 2002). Thus, although linear elastic boundary element method simulations provide useful insights into the mechanics of fault interaction, these models are not able to reproduce in detail the bed geometries and therefore displacement distributions associated with natural relay zones.

Peacock and Zhang (1994) were the first authors to study the kinematics of fault segment interaction using distinct element method simulations. Their models, based on a two-dimensional (2-D) code ('Universal Distinct Element Code' [UDEC]; Cundall, 1971) which simulates brittle rocks as regularly packed arrays of elastic–plastic blocks that are free to slide past each other, were designed to investigate the effects of lithological layering on deformation in contractional and extensional oversteps along normal faults (e.g. Peacock and Sanderson, 1992). However, as Peacock and Zhang (1994) have pointed out, a major limitation of UDEC is that the locations/orientations of potential breaching faults are pre-determined by the regular packing geometry of the elastic–plastic blocks within brittle layers. It is the continuing improvement in computing power and the advent of PFC^{3D} that have allowed us to go beyond these earlier studies by developing 3-D models that incorporate incremental strain accumulation and realistic fault propagation (cf. Strayer and Suppe, 2002).

3. Methodology

3.1. Distinct element method

The distinct element method simulates the behaviour of elastic particles that interact at point contacts under the effect of specified force or displacement boundary conditions (Cundall and Strack, 1979; Fig. 2a). In PFC^{3D}, interactions between spherical particles ('balls') are controlled by their normal and shear stiffnesses and, in the case of non-bonded particles, by a Coulomb friction law applied at ball–ball interfaces (Fig. 2). The stiffnesses are scaled according to particle size. An explicit finite difference algorithm simultaneously solves the equations of motion and the force-displacement law to calculate, respectively, the ball positions in *xyz* space and the normal and shear forces acting at each contact (Itasca Consulting Group, 1999b; see Cundall and Strack (1979) for an accessible

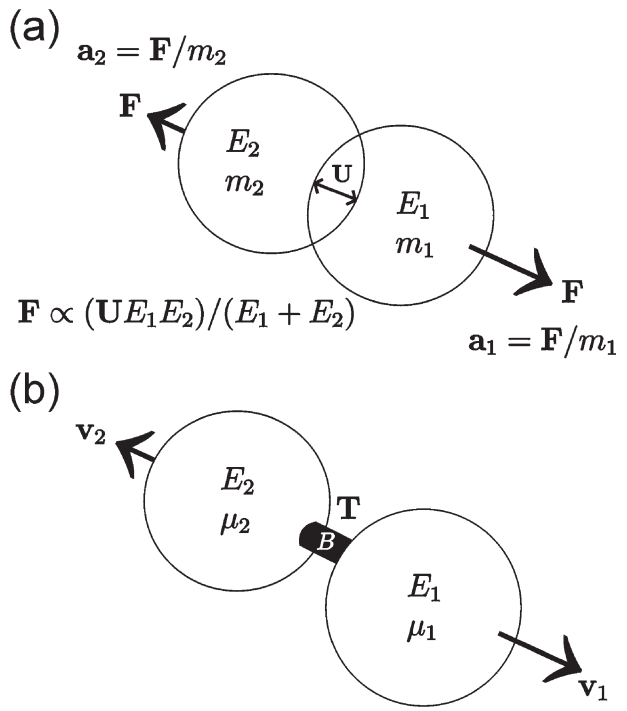

Fig. 2. Principles of the distinct element method as implemented in PFC^{3D}. (a) Schematic diagram showing spherical particles interacting at their contacts. The contact force (**F**) between two particles depends on the amount of overlap (**U**) and the contact moduli (E_1 and E_2). The size of the overlap has been exaggerated for clarity. In reality, the particles overlap at point contacts with vanishingly small areas; volume is therefore conserved. The acceleration also depends on the mass of each particle (m_1 and m_2). (b) Contact bond between two particles (B) resists tensile forces (**T**). Where the bonds are broken or for unbonded particles, frictional sliding between the particles depends on the surface friction coefficients (μ_1 and μ_2).

description of the DEM formulation). To ensure numerical stability, a time step, which depends on ball stiffness and density, is calculated for each particle in the model and a critical time step is chosen such that a mechanical disturbance cannot propagate further from any particle than its immediate neighbours during each calculation cycle. The consequences of this time stepping scheme for modelling fault systems to high finite shear strains are discussed below (Section 3.2).

The particles can be bonded together at point contacts to simulate the behaviour of a cohesive rock ('bonded particle model'; Hazzard et al., 2000; Fig. 2b). No inter-particle slip is allowed where a contact bond exists. A contact bond breaks when its shear or tensile strength is exceeded (Itasca Consulting Group, 1999b) and there is no healing of bonds in the models described here. The normal and shear strengths assigned to individual contact bonds are drawn at random from a normal distribution and then scaled according to particle size. The resulting spatial distribution of bond strengths has important consequences for the way in which the model relay zones grow and breach (Sections 4.1 and 4.3). Simulated bi- and triaxial core tests have shown that bonded particle models successfully reproduce the macroscopic stress–strain behaviour of naturally occurring sedimentary (sandstone and chalk) and crystalline (granitic) rocks (Hazzard, 1998; Hazzard et al., 2000). Particle stiffness and the normal/shear stiffness ratio were found to influence the Young's modulus and Poisson's ratio, respectively, whilst the Gaussian contact bond strength distribution controls the strength of the bulk PFC material. Thus, the macroscopic behaviour of PFC materials is controlled by the micro-parameters assigned to individual particles (Itasca Consulting Group, 1999a,c; Hazzard et al., 2000). Recent studies have shown that strain localization is possible in the post-peak strength regime given a large number of particles, appropriate boundary conditions and sufficient strain (Antonellini and Pollard, 1995; Morgan and Boettcher, 1999; Strayer and Suppe, 2002; Finch et al., 2003). Crucially inelastic (i.e. permanent) strains can develop prior to macroscopic failure, or in the case of the models presented here, prior to relay breaching, by bond breakage and particle rotations and translations. It is this behaviour that makes PFC^{3D} an ideal tool to investigate the kinematics of fault linkage.

3.2. Experimental set-up

The relay models are based on compact, bonded cubes comprising ca. 71,500 balls and measuring $50 \times 50 \times 50$ units (model scaling is discussed below). We ran simulations using three different cubes in order to test the sensitivity of relay breaching to variations in ball packing geometry. The cubes comprise an assemblage with a uniform particle size distribution (PSD) with maximum and minimum ball sizes of 0.83 and 0.5 units, respectively, and two assemblages that represent different realizations of a power-law PSD which has an exponent of 2.6 and is defined by particles belonging to one of four size classes (radii of 0.675, 0.45, 0.3 and 0.2 units). Previous work (Morgan, 1999; Morgan and Boettcher, 1999) has shown that strain localization in 2-D granular materials is enhanced if the power-law exponent of the PSD is ≥ 1.6. An equivalent, 3-D exponent of 2.6 was therefore selected to facilitate strain localization during relay breaching.

The cubes were created by placing, at random, the specified number of particles drawn from either the uniform or power-law PSD at half their final radii into a $50 \times 50 \times 50$ unit volume bounded by six frictionless, elastic walls. The particles were then expanded to their required sizes and the assemblage was allowed to reach static equilibrium i.e. the out-of-balance forces acting on the particles were minimized (Strayer and Suppe, 2002). 'Floating' particles with fewer than three contacts (generally $\ll$ ca. 10% of the total number of particles) were then expanded and bonds were installed at the newly created contacts to ensure that a dense network of contact bonds was produced during the bond installation step. This procedure resulted in a compact, low porosity assemblage with no significant structural/mechanical anisotropy (see Itasca Consulting Group, 1999c). The particle micro-parameters

were then calibrated in a simulated triaxial testing rig (Strayer and Suppe, 2002) to reproduce the bulk properties of a typical fine-grained sandstone, the Springwell sandstone (Wu et al., 1991; Hazzard, 1998), deformed under a confining pressure of ca. 30 MPa equivalent to a depth of approximately 1 km in the crust (Table 1). Finally, the walls surrounding the calibrated sandstone cube were deleted and an inward-directed force of 10^6 N was applied to all particles on the boundaries of the model to provide the required isotropic confining pressure. We can estimate the physical dimensions of the assemblage by comparing the magnitude of the inward-directed force acting across each face with the confining pressures expected at depths of ca. 1 km. The force/pressure ratio implies that the linear dimensions of a $50 \times 50 \times 50$ unit cube are between 15 and 20 m and suggests that individual particles have radii of a few tens of centimetres. Gravitational (i.e. isostatic) effects are unlikely to influence relay growth and breaching on this sub-seismic scale and hence have not been incorporated into our models.

In order to obtain maximum resolution in the relay ramp whilst, as far as possible, minimizing the boundary effects caused by the fault tip-lines interacting with the faces of the cube, we have chosen to model a rock volume containing two vertical discontinuities that represent 'patches' on two overlapping, vertical fault segments whose notional upper and lower tip- (or branch) lines lie above and below the upper and lower boundaries of the model, respectively (Fig. 3). A similar conceptualization was used by Walsh et al. (2001) to model the kinematics of a normal fault array comprising eight or nine individual faults. The fault patches are defined by 'fault balls' with zero bond strength and whose elastic stiffnesses and radii were reduced by factors of 2 and 1.25, respectively, relative to particles in the sandstone matrix. These factors were chosen such that the numerical time steps calculated for the fault balls are not significantly different to the time steps calculated for particles in the sandstone matrix. The strength of the faults is controlled by the elastic stiffnesses of the particles along and on either side of each discontinuity and the reductions in stiffness and radii allow easy slip on the faults permitting fault interaction soon after the onset of deformation (Walsh et al., 2001; Section 4.1).

The models were loaded by applying equal and opposite velocities parallel to the z-axis to all particles on either fault-parallel face of the cube (Fig. 3c). This shear boundary condition partitions equal amounts of displacement between 'footwall' uplift and 'hanging wall' subsidence. Though the elastic deformation fields adjacent to naturally-occurring, large normal faults are often asymmetric, i.e. hanging wall subsidence > footwall uplift (e.g. Stein and Barrientos, 1985), this asymmetry is usually attributable to free surface effects in dipping normal faults, with vertical free surface intersecting faults and small blind faults having symmetrical deformation fields (e.g. Gibson et al., 1989). The fault patches modelled here, which are subject to a constant lithostatic, (i.e. confining) pressure (see above), can therefore be taken to be equivalent to segments on a small blind normal fault. The shear boundary condition, though simple, allows realistic, symmetric deformation fields to develop adjacent to the relay bounding faults and, most importantly, permits non-plane strain (i.e. fully 3-D) deformation within the relay ramp (Section 4).

The faults lie parallel to the shear plane, a configuration that, in principle, allows large fault displacements to accumulate. However, the time stepping scheme used by PFC^{3D} (Section 3.1) means that the system responds to 'high' and 'low' boundary velocities by partitioning different amounts of displacement between localized slip on the faults and distributed shear within the footwall and hanging wall blocks. At 'low' boundary velocities ($\leq 5 \times 10^{-6}$ units per time step), the amount of distributed shear strain is low hence the maximum displacement on each fault (i.e. the displacement measured outside the relay zone) is nearly equal to the displacement measured at the boundaries of the model. At higher boundary velocities, however, the distributed shear strain accommodates more than half the displacement across the boundaries of the model (Fig. 4b). Distributed shear strain in the footwall and hanging wall blocks is accommodated by mainly elastic deformation leading to significantly higher out-of-balance forces in models loaded with 'high' boundary velocities compared with models loaded with 'low' boundary velocities (Fig. 4c). Thus, models loaded with boundary velocities less than 5×10^{-6} units per time step are, in principle, optimal for the purposes of studying fault segment interaction. However, in simulations conducted on a Windows® NT server (700 MHz Pentium® III processor/1024 Mb RAM), relays loaded using a low boundary

Table 1
PFC^{3D} microparameters and bulk properties of the model sandstones. Min. radius = minimum particle radius (model units); radius ratio = ratio between maximum and minimum particle radii (for model with a uniform PSD); contact modulus = ball–ball contact modulus (MPa); stiffness ratio = ratio between particle normal and shear stiffnesses; mean norm. strength = mean normal strength of contact bonds (MPa) (standard deviation in brackets); mean shear strength = mean shear strength of contact bonds (MPa) (standard deviation in brackets); E = bulk Young's modulus (MPa); υ = Poisson's ratio; UCS = unconfined compressive strength (MPa). Microparameters for the Springwell sandstone are from Hazzard (1998)

	Min. radius	Radius ratio	Contact modulus (MPa)	Stiffness ratio	Mean norm. strength (MPa)	Mean shear strength (MPa)	E (MPa)	υ	UCS (MPa)
Springwell	0.5	1.66	2.78E4	5.5	35.1 (31.8)	47.7 (31.8)	1.14E4	0.32	34.3
Navajo	0.5	1.66	1.26E5	16.2	170.0 (50)	170.0 (50)	3.4E4	0.36	169

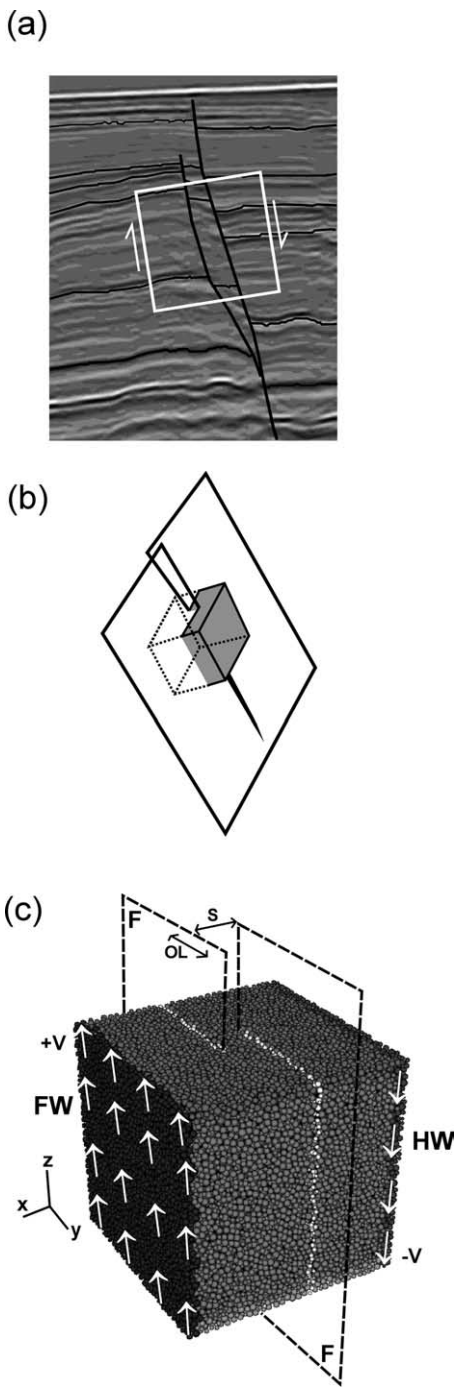

Fig. 3. (a) Seismic section and (b) schematic block diagram through a relay zone showing the volume around two overlapping faults. We assume that the boundary conditions applied to the volume surrounding a relay zone (box) can be approximated by simple shear. In (b), the hanging wall block is shaded. (c) Starting assemblage with a uniform particle size distribution comprising ca. 71500 balls. The cube is cut by two overlapping, parallel faults (white balls) that represent small patches on two larger fault segments (F). OL = overlap length; S = fault separation. Equal and opposite velocities (+V/−V) are applied to all particles on the fault-parallel faces of the cube (dark grey balls); FW = footwall block, HW = hanging wall block. An inward-directed force is applied to all particles on each face of the cube. The approximate linear dimensions of the unit cube are estimated to be between 15 and 20 m such that individual particles therefore have dimensions of a few tens of centimetres (see text).

velocity ($\leq 5 \times 10^{-6}$ units per time step) required between 1 and 2 weeks to reach the point of breaching. A more practical solution is to shear the model for 2500 time steps with a 'high' velocity of 5×10^{-5} units per time step, then 'freeze' the boundaries (i.e. set the boundary velocity to zero whilst maintaining the displacement) and allow the elastic strains that accumulate in the footwall and hanging wall blocks to be converted into permanent displacements on the faults. The boundary velocities are then re-imposed for a further 2500 steps. Several loading cycles are required to reach the point of relay breaching, which typically takes between 4 and 7 days. Though there is no timescale implicit in the DEM formulation, the simulations must represent a sufficiently long period of time to allow the elastic strains in the rock volume to be converted into permanent displacements, including the generation of inelastic strains within the relay zone, by bond breakage and particle rotations/translations, prior to breaching.

The out-of-balance forces developed in models with a 'high' boundary velocity (5×10^{-5} units per time step) are, on average, within a factor of two of those developed in 'low' constant velocity (5×10^{-6} units per time step) models, but are nearly five times lower than the out-of-balance forces developed in 'high' constant velocity (5×10^{-5} units per time step) models (Fig. 4c). Crucially, we have found no significant differences in the ramp geometries or strains at breaching between the cyclic loading and low constant velocity models, giving us confidence that this boundary condition does not introduce spurious forces into the numerical solution (Fig. 4d).

The simulations were allowed to develop until the total displacement measured across the model boundaries (hereafter referred to as 'boundary displacements') reached ca. 11 units, equivalent to a maximum fault displacement of less than 5 m ($\approx$25% of the cube dimensions). Particle displacements in three initially horizontal marker horizons with no mechanical significance were recorded every 0.27 units of boundary displacement to determine the slip distribution on the faults and the strain in the relay ramp. We investigated the growth and breaching of relays with an aspect ratio of one (separation = overlap = 8.33 units $\approx$4 m) using the three realizations of the Springwell sandstone cube and one additional model of Navajo sandstone (Table 1). A detailed description of relay growth and breaching for a relay zone in a Springwell sandstone cube with a power-law PSD is presented below. We summarize the main features of growth and breaching for the model relay zones and summarize the effects of PSD on relay breaching in PFC^{3D} models.

4. Results

4.1. Relay zone geometry and displacement transfer

Fig. 5a is a horizon map from the centre of a typical

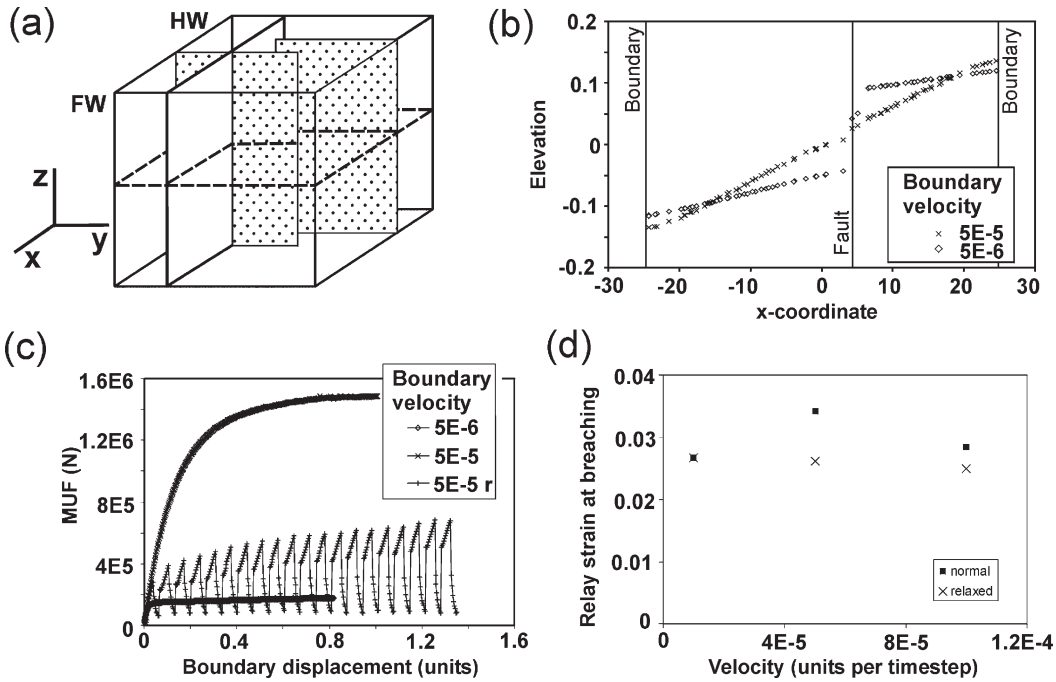

Fig. 4. (a) Schematic diagram of the starting assemblage showing the pre-defined faults (stippled), a reference horizon (dashed lines) and a vertical *xz* slice through the model (solid lines). FW = footwall block; HW = hanging wall block. (b) Graph showing the elevations of particles that were originally located at the intersection between the reference horizon and *xz* slice in (a) vs. *x*-coordinate for two models loaded with boundary velocities of 5×10^{-5} and 5×10^{-6} units per time step after ca. 0.27 units of boundary displacement (ca. 0.13 m). (c) Graph showing mean unbalanced force (MUF) vs. boundary displacement for models loaded with constant boundary velocities of 5×10^{-5} and 5×10^{-6} units per time step, and a cyclic loading model (see text) with a velocity of 5×10^{-5} units per time step ('5E − 5 r'). (d) Graph of fault-parallel shear strain in the relay ramp (i.e. relay strain) at the point of breaching vs. boundary velocity for models loaded with a constant velocity ('normal') and a cyclic loading boundary condition ('relaxed'). The microparameters assigned to particles in this 'test' model were the same as those listed for Springwell sandstone in Table 1 apart from the following: contact modulus = 7.83E3 MPa; mean normal strength = 1.8 MPa; mean shear strength = 1.26 MPa. This model illustrates that the effect of the lower contact modulus and normal/shear contact bond strengths relative to those of the Springwell sandstone models is to reduce the amount of strain required for relay breaching.

PFC^{3D} simulation after 0.27 units (ca. 0.13 m) of boundary displacement (boundary displacement ca. 3.2% of the fault separation). The horizon, which was originally planar, has been offset across the two faults. The structure contour pattern shows that the horizon is gently inclined within the footwall and hanging wall blocks indicating that most of the displacement (ca. 90%) has been accommodated by slip on the faults rather than by distributed shear strain within the cube. Within the overlap zone, the structure contours are closely spaced and approximately orthogonal to the trace of the pre-defined faults but are more widely spaced and oblique to the faults in the regions adjacent to, and beyond the fault tips. These observations show that a ramp, which connects the footwall and hanging wall blocks, has developed after 0.27 units (ca. 0.13 m) of boundary displacement. The ramp dip direction is parallel to the strike of the faults within the overlap zone, but also has a component of dip down towards the hanging wall in the regions adjacent to and beyond the fault tips, thus defining a rhomb shape in map view (Fig. 5a). Relay shape can be quantified by the ratio of the fault transfer length to fault overlap length (TL:OL; Fig. 1b and c). TL:OL = 1 indicates that the relay ramp is square in map view; TL:OL > 1 implies that the relay is rhomb-shaped. For the horizon shown in Fig. 5a, TL:OL = 2.

A separation diagram of the horizon cutoffs against the two faults (Fig. 5b) shows that displacement on the footwall fault decreases from ca. 0.25 units (≪ ca. 0.12 m which is 3% of the fault separation) at $y = -11$ units to zero at $y = 5$ units whilst the displacement on the hanging wall fault decreases from ca. 0.25 units at $y = 11$ units to zero at $y = -8$ units. The decrease in displacement on the footwall fault is therefore matched by a complementary increase in displacement on the hanging wall fault and the ramp transfers displacement from the footwall fault onto the hanging wall fault, i.e. the rock volume between the two faults is a relay zone. The rock volumes immediately outside the relay zone accommodate low shear strains (γ) of ca. 1×10^{-2} and 1×10^{-3}, respectively, in the directions normal and parallel to the trace of the faults (Fig. 5b). The magnitude of the fault-normal component of shear strain is greatest at the fault tips and decreases towards the model boundaries. It is these zones of deformation beyond the fault tips that give rise to the oblique structure contours observed in Fig. 5a. Inspection of Fig. 5b shows that the faults have propagated beyond their pre-defined tips, with an increase in fault length on each segment equivalent to ≤ ca. 30% of the original overlap length (ca. 1.2 m). Despite this propagation, the finite displacement profiles within the relay zone are approximately linear (Fig. 5c; see also Section 4.2 and

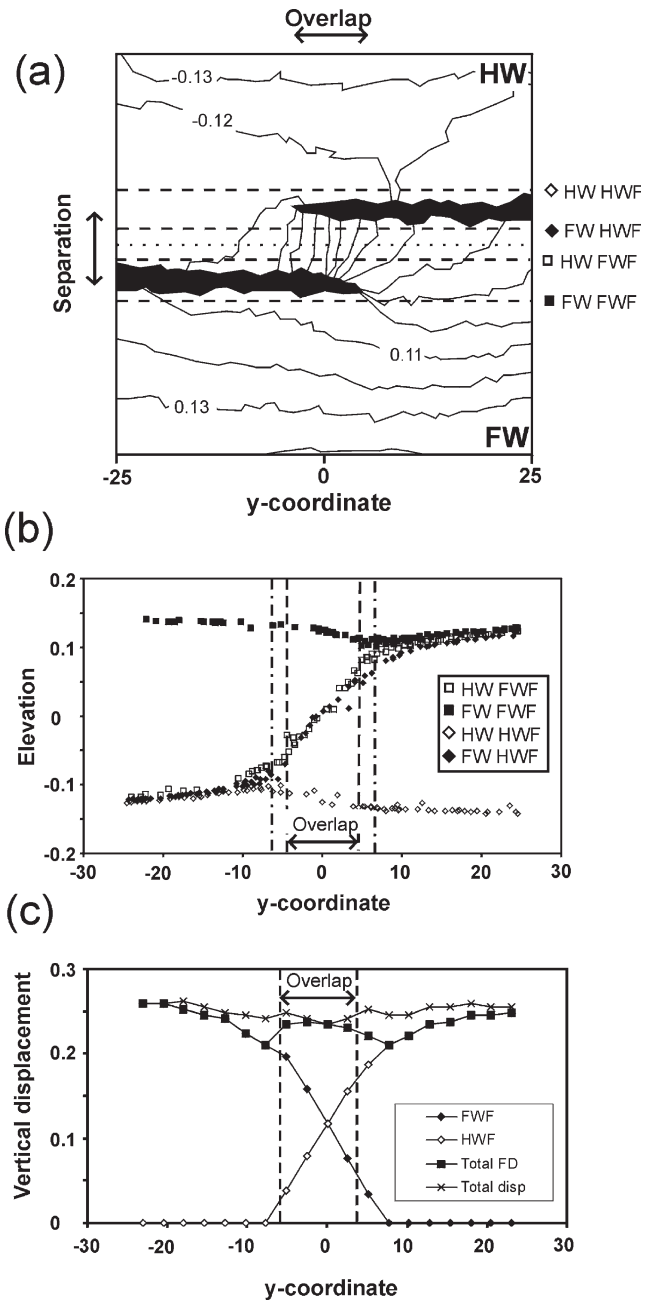

Fig. 5. (a) Structure contour map of the reference horizon in Fig. 4a after ca. 0.27 units of boundary displacement. The contours show elevation above a starting datum, which is assumed to be zero. The contour interval is 0.01 units and the traces of the pre-defined faults are shown in black. FW = footwall; HW = hanging wall. The dashed lines show the locations of the footwall and hanging wall cutoffs illustrated in (b). The square/diamond symbols correspond to the symbols used in (b). The dotted line shows the location of the profiles illustrated in Fig. 6a. (b) Separation diagram for the same reference horizon showing the hanging wall cutoffs against the footwall fault (HW FWF), the footwall cutoffs against the footwall faults (FW FWF), the hanging wall cutoffs against the hanging wall fault (HW HWF) and the footwall cutoffs against the hanging wall fault (FW HWF). Note that the diagram is oriented so that the reader is looking from the footwall towards the hanging wall. The vertical dashed lines show the pre-defined fault overlap length and the original position of the fault tips. The vertical dot–dash lines show the new position of the fault tips following fault propagation at the onset of deformation. See text for explanation. (c) Displacement profiles for the reference horizon in Fig. 4a showing the vertical component of displacement on the footwall fault (FWF) and hanging wall fault (HWF). 'Total FD' = FW fault displacement + HW fault displacement. 'Total disp' = 'total FD' + vertical shear accommodated by distributed deformation around the fault tip-lines. All results are presented in model units; 1 model unit is ca. 0.5 m (see text).

Fig. 6a). This linearity is consistent with fault propagation having occurred during the earliest stages of deformation, i.e. at boundary displacements $<<0.27$ units. Tip propagation at the earliest stages of deformation is most likely if the pre-defined fault tip-lines intersect contact bonds that were assigned strengths drawn from the lower end of the Gaussian bond strength distribution (Section 3.1). Such bonds will fail under lower applied loads—and therefore at lower strains—than contact bonds that were assigned strengths drawn from the middle to upper end of the Gaussian bond strength distribution. Fault tip propagation during the earliest stages of deformation is, therefore, more likely to reflect the inherent, particle-scale heterogeneity of the PFC^{3D} model rather than any fundamental aspect of fault segment interaction.

The *total* fault displacement (i.e. the sum of the slip on the footwall and hanging wall faults) is nearly constant across the model apart from two 'lows' coincident with the fault tips. If the displacement accommodated by distributed shear in the volumes surrounding the fault tip-lines is added to the total fault displacement, the aggregated displacement profile is approximately equivalent to that of a single, through-going fault surface (Fig. 5c). These observations show that the faults are geometrically coherent at low boundary displacements.

4.2. Growth of intact relays

Fig. 6a shows a series of profiles from the footwall, down the centre of the relay ramp into the hanging wall block for the same model at different boundary displacements. The ramp is approximately planar within the fault overlap and the dip of the ramp is greater in models with high boundary displacements than in models with low boundary displacements. For intact relays, there is a near linear relationship between fault-parallel shear strain in the relay ramp ('relay strain') and boundary displacement (Fig. 6b). Since there is no evidence to suggest that the faults have propagated beyond the tip-lines established during the first increments of deformation (Section 4.1), intact relay zones 'grow' by ramp rotation. The relay strains obtained from the three different Springwell sandstone model relay zones are shown in Fig. 6c. Two of the simulations were based on assemblages with power-law particle size distributions ('pldist2b' and 'sppl1b'); the other simulation was based on an assemblage with a uniform PSD ('uniform'). Fig. 6c shows that the relay strains increase linearly with boundary displacement until the relay zone is fully hard linked

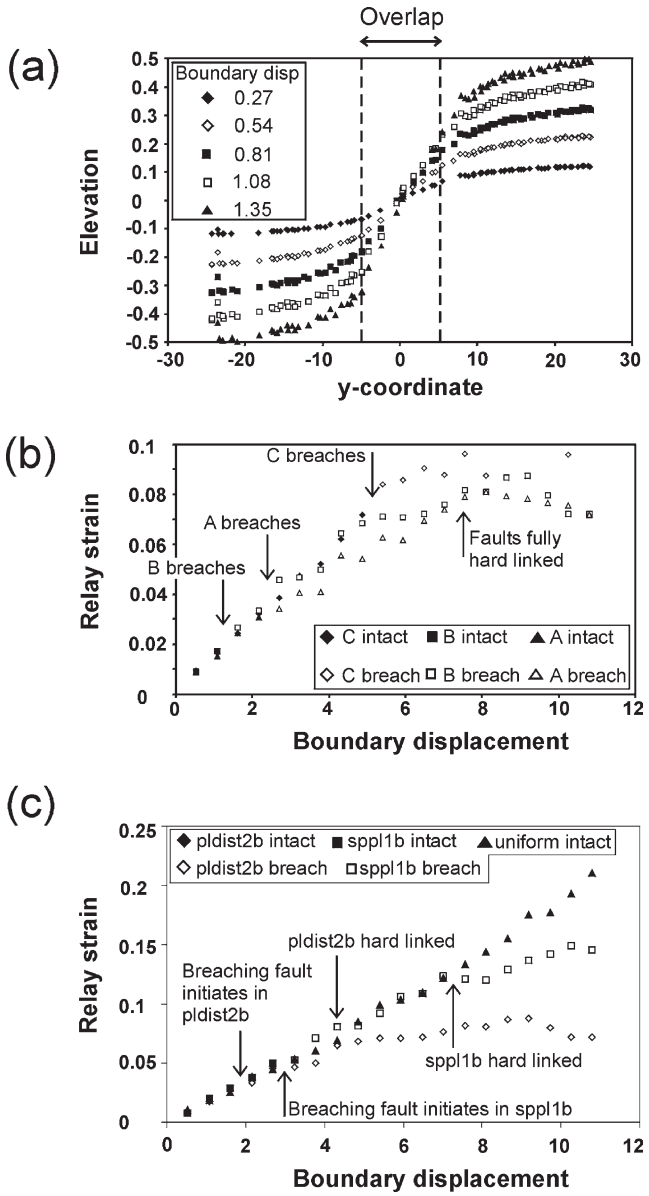

Fig. 6. (a) Graph showing the elevations of particles in the centre of the same relay ramp at different boundary displacements between 0.27 and 1.35 units. See Fig. 5a for the location of these profiles. The starting elevations of all these particles are set to zero. (b) Graph showing fault-parallel shear strain ('relay strain') accommodated by the relay ramp on three different horizons (A, B, C—see Fig. 8a, inset) versus boundary displacement. Filled symbols indicate that the relay ramp is intact on that particular horizon; open symbols indicate that the relay ramp has been breached on that particular horizon. (c) Graph showing fault-parallel shear strain accommodated by relay ramps in two assemblages with power-law particle size distributions ('pldist2b' and 'sppl1b') and in an assemblage with a uniform PSD ('uniform'). Filled symbols indicate that the relay ramp is intact on a particular horizon; open symbols indicate that the relay ramp has been breached on that particular horizon. Note that the relay in the assemblage with a uniform PSD does not reach the point of breaching. All results are presented in model units; 1 model unit is ca. 0.5 m (see text).

(Section 4.3). The relay strains obtained from intact relays in the model with a uniform PSD are higher than the relay strains obtained from intact relays in the models with power-law particle size distributions. These observations

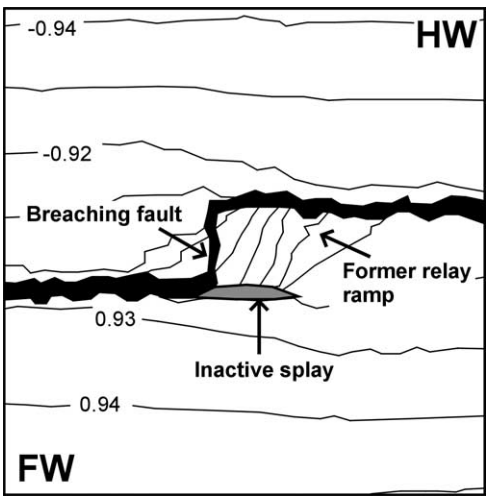

Fig. 7. Structure contour map of the reference horizon in Fig. 4a after ca. 2 units of boundary displacement showing a hanging wall breached relay. The contours show elevation above and below a starting datum, which is assumed to have been zero. FW = footwall; HW = hanging wall. One model unit is ca. 0.5 m (see text).

show that relay zone models based on assemblages with uniform particle size distributions breach at higher relay strains (a factor of two higher) than models based on assemblages with power-law particle size distributions; a feature that is consistent with the increased localization of materials with power-law particle size distributions (Morgan, 1999; Morgan and Boettcher, 1999).

4.3. Relay breaching

Fig. 7 is a horizon map from the centre of a typical model after ca. 1.9 units of boundary displacement (boundary displacement ≈23% of the fault separation). Displacement localization distinguishes the breaching fault from the zones of distributed deformation beyond the tips of the relay-bounding faults (e.g. Fig. 5a). The breaching fault is oriented sub-perpendicular to the trace of the bounding faults and cuts across the bottom of the relay ramp to produce a hanging wall (i.e. lower-ramp) breached relay (Childs et al., 1995; Crider, 2001). The former relay ramp and associated inactive or abandoned splay fault are preserved in the footwall of the through-going fault (Fig. 7). Of the four models presented here (Section 3.2), three of the relays failed by hanging wall (i.e. lower-ramp) breaching and one by footwall breaching; for these models and several layered models not described here ($n = 14$) we have yet to see a breaching fault that cuts through the centre of a relay ramp. There is no asymmetry to the cyclic loading boundary condition (Section 3.2), which suggests that whether a relay ramp fails by hanging wall or footwall breaching may be due to particle-scale heterogeneities in the PFC^{3D} model (Section 4.1). We anticipate that analysis of a large number of simulations based on starting assemblages with a wider range of PSDs than were tested here (i.e. $>>3$)

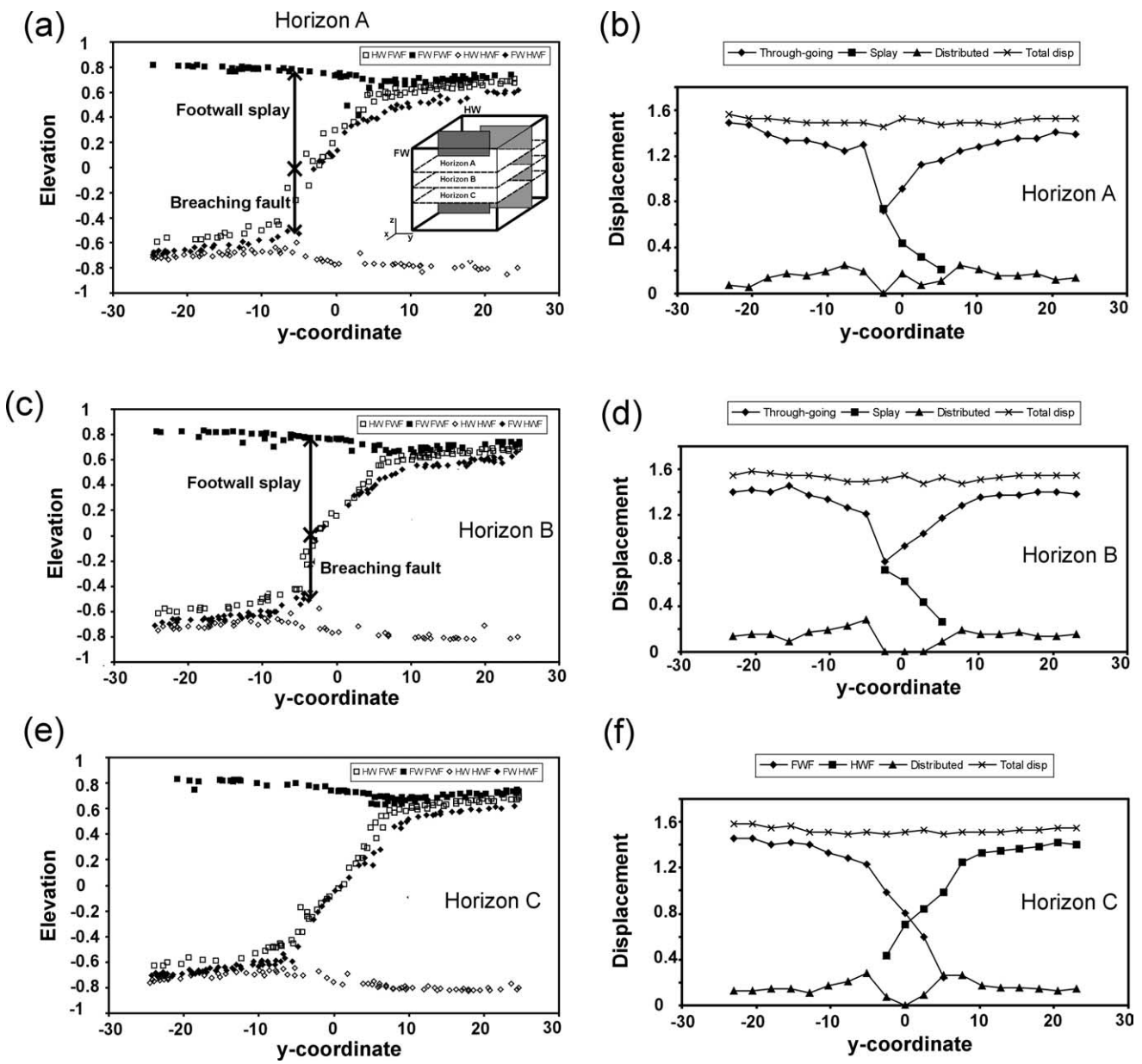

Fig. 8. Horizon separation diagrams ((a), (c) and (e)) and displacement profiles ((b), (d) and (f)) for Horizons A–C (shown in inset). The key to the separation diagrams is the same as in Fig. 5b. The displacement profiles in (b) and (d) show the displacement on the through-going fault surface, the displacement on the footwall splay fault, the vertical shear accommodated by distributed deformation around the fault tip-lines and the sum of these three components. The displacement profiles in (f) are for the displacement on the footwall fault (FWF), the displacement on the hanging wall fault (HWF), distributed shear and the sum of these components. All results are presented in model units; 1 model unit is ca. 0.5 m (see text).

would yield a ratio of hanging wall to footwall breached relays of approximately 1:1. A displacement profile for a typical hanging wall breached relay shows that the displacement on the through-going fault decreases to a minimum at the branch-line between the breaching fault and the footwall splay (Fig. 8d). However, if the displacements accommodated on both the inactive splay and in the rock volumes beyond its tip-line are added to the slip on the through-going fault, the total displacement is nearly constant across the entire model (Fig. 8d). Thus, the breaching fault transfers displacement across the failed relay at the level of the mapped horizon.

Horizon separation diagrams of the cutoffs at three different levels on the relay-bounding faults (Fig. 8a, c and e) show, however, that the relay zone is not fully hard linked: the relay ramp appears to be intact below the centre of the model (Horizon C, Fig. 8e and f). Analysis of the relay strains and breaching fault displacements at different stages during the development of this relay zone shows that the breaching fault began to localize on certain levels within the model when the strain reached ca. 0.02 (equivalent to a ramp dip of ca. 1°), though the bounding faults did not become fully hard linked in 3-D until the relay strain had increased to ca. 0.08 (equivalent to ramp

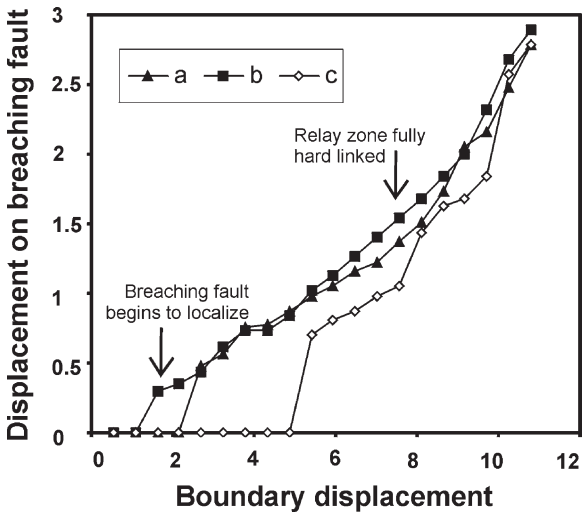

Fig. 9. Graph showing breaching fault displacement vs. boundary displacement for the three horizons in Fig. 8 (inset). The faults are considered fully hard linked when the relay ramp is breached on all three measurement horizons (Fig. 8) and at the top and base of the model.

dip ca. 4.6°; Fig. 6b). Following 3-D hard linkage, the relay ramp strain remained more-or-less constant with increasing boundary displacement (Fig. 6b). The displacement on the breaching fault, however, increased continuously with increasing boundary displacement (Fig. 9). These observations show that: (1) breaching fault propagation, and therefore hard linkage in 3-D, are not instantaneous; (2) displacement transfer in 'partially breached' relays (i.e. those relay zones in which a breaching fault has localized at certain levels within the models, but are not yet fully hard linked in 3-D) is accommodated by ramp rotation *and* slip on the incipient breaching fault; (3) displacement in fully hard linked relay zones is accommodated by slip on the through-going fault, the inactive relay ramp and associated splay fault being carried passively in the footwall or hanging wall of the through-going fault surface. Although the strains in partially breached relay zones are likely to be complex owing to the partitioning of displacement between ramp rotation and slip on the incipient breaching fault, displacement profiles for the three horizons in the partially breached relay in Fig. 8 show that the *total* displacement (i.e. breaching fault displacement + displacement on the footwall splay + distributed strain at the fault tips) is the same at all levels within the model. The overall effect, therefore, is to maintain geometric coherence between the overlapping fault segments at all levels in the model.

5. Comparison with natural relays

An important test of the 'validity' of the numerical modelling results is how closely the models reproduce features seen in natural relay zones (cf. Crider and Pollard, 1998). In the following section, we compare the geometries,

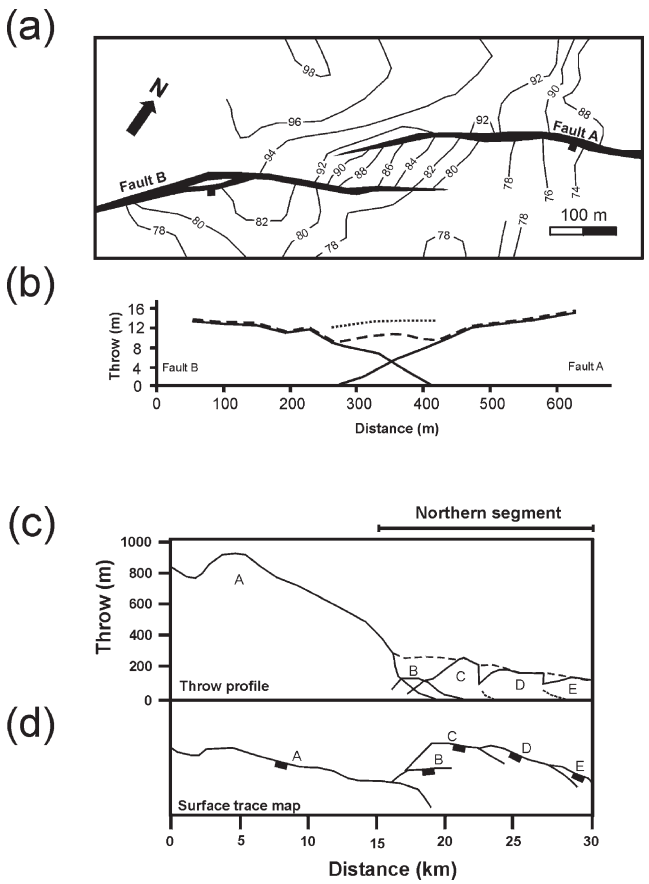

Fig. 10. (a) Map of an intact relay ramp at the Daisy Hill opencast coal site, Northumberland, after Huggins et al. (1995). Fault segments 'A' and 'B' cut the Main Seam (seam elevation contours in metres) and down throw towards the SE (black boxes). (b) Throw profiles (solid lines) for fault segments 'A' and 'B' in (a); aggregate fault throw (dashed line); aggregate throw including the ductile shear strain component (finely dashed line). (c) Throw profiles of footwall breached relays between fault segments 'C', 'D' and 'E' along the northern segment of the Moab Fault, Utah, after Foxford et al. (1998). Profiles show throws on the through-going fault (solid line); throws on the hanging wall splay faults (finely dashed lines); total fault throw (dashed line). (d) Surface trace map showing the fault segments labelled in (c).

displacement transfer characteristics and strains obtained from the numerical simulations with those from natural relay zones.

Fig. 10a shows a relay ramp on a normal fault that cuts well-bedded sandstones and shales (Huggins et al., 1995). This relay zone, which is typical of neutral relays on normal faults that offset sub-horizontal sedimentary sequences, is characterized by: (1) a rhomb-shaped relay ramp with a component of dip towards the hanging wall (TL:OL = 1.4; Fig. 10a); (2) approximately constant throw gradients within the relay zone (Fig. 10b); (3) an aggregated displacement profile (i.e. total fault displacement + down-to-the-hanging wall component of shear strain) equivalent to that of a single fault (Fig. 10b). The PFC^{3D} models described in Sections 4.1 and 4.2 reproduce the features of this intact relay (Fig. 5). Crucially, the modelled relay ramps dip towards the hanging

wall, which suggests that the PFC^{3D} models capture the mechanics of fault segment interaction during incremental slip accumulation in a more realistic manner than linear elastic boundary element method simulations (Willemse et al., 1996; Willemse, 1997; Crider and Pollard, 1998).

We have, for the first time, been able to model the propagation of relay bounding faults and relay breaching. The models described in Section 4.3 (Figs. 7 and 8) reproduce the characteristic geometries and displacement profiles of natural breached relays (Fig. 10c), including: (1) breaching faults that cut across the hinges (not the middle) of the relay ramp (Fig. 10d); (2) displacement minima at the branch-lines between the inactive splay faults and the through-going fault surface (Fig. 10c); (3) smooth aggregated displacement profiles (Fig. 10c). These observations suggest that fault localization, propagation and displacement accumulation within the models are sufficiently realistic that we can model the kinematics of relay breaching without having to 'seed' a breaching fault at the start of the simulation (cf. Peacock and Zhang, 1994). Thus, distinct element method simulations potentially offer a basis for predicting the likelihood of relay breaching. A key question, therefore, is how well do the modelled breaching strains compare with the strains recorded in natural relays?

We have collated a dataset of strains in natural breached relay zones from outcrop and seismic data. The dataset comprises some structures for which fault displacements can be backstripped to the point of breaching so that the relay strain at the time of breaching can be measured; however, for the majority of data only the present day displacement distribution is known. In these latter cases we have measured the relay breaching strain from the dip of the relict, inactive relay ramp relative to the regional dip measured parallel to the bounding faults. These breaching strain measurements are based on the assumption that ramp rotation ceased following relay breaching. Although the numerical models described here suggest that the strain at which a relay zone is breached in 3-D may be up to twice the strain at breaching on an individual plane of observation, potential errors due to this assumption do not effect our comparisons with model data as these are similarly measured from map sections through 3-D structures. Our dataset of relay breaching strains from the numerical models is derived from measurements on three observation horizons (e.g. Fig. 8) in the Navajo sandstone model and three observation horizons in each of the three Springwell sandstone models (Fig. 8).

The majority of relay breaching strains from the natural data lie within the range 0.02–0.3 (Fig. 11a), corresponding to fault parallel ramp dips of between 1 and 22°, and have a mean value of 0.13. The strains measured from the model relays have a more limited range with a lower mean value of 0.085 but nevertheless compare favourably with strain magnitudes in natural structures. The lower mean breaching strains for the model relay zones can partly be attributed to the homogeneity of the model sequence. The models were based on massive Springwell sandstone blocks (the dimensions of each block being more than six times the fault separation; Section 3.2), whereas the natural data include relays in relatively thinly bedded sedimentary sequences. Recent studies suggest that relay zones on faults that cut massive host rocks are more likely to be hard linked than neutral relay zones on normal faults that cut horizontally bedded sequences because the shear strains in the former cannot be accommodated by bed-parallel slip (Walsh et al., 1999). Thus, the modelled relay strains are consistent with the massive nature of the sandstone host rocks.

Analysis of the collated natural dataset demonstrates that the ratio between relay zone separation and fault transfer throw on relay bounding faults is higher for breached relay zones than for intact relay zones (Fig. 11b). This observation provides a basis for estimating the probability that a relay zone of a given separation will breach at a particular throw (Fig. 11c). Although the size of our model dataset for homogeneous starting sandstone cubes is limited, the range of ratios of relay separation to throw over which breaching occurs is similar to the natural dataset. As well as inspiring confidence in the ability of our numerical models to replicate natural relay zones in both qualitative and quantitative aspects, these analyses may provide a basis for developing predictive methods in a variety of application areas; such as, prediction of the preservation potential of sub-seismic relay zones in the risking of fault traps.

6. Discussion

Distinct element models are capable of reproducing many of the geometric and kinematic features of relay zones embodied in existing conceptual models (e.g. Peacock and Sanderson, 1994; Childs et al., 1995). Early stage growth is characterized by a stable relay ramp configuration with progressive ramp rotation as displacement accumulates. Ramp rotation is eventually followed by ramp breaching along the hinges of the relay ramp, with subsequent displacement localizing on the through-going fault at the expense of an inactive hanging wall or footwall splay. Although our modelling predicts strains associated with relay breaching that are broadly equivalent to those observed in nature, there are several features not included in the models that could be critical to relay evolution. For example, our models only examine the evolution of relay zone geometries with a given aspect ratio and with parallel bounding fault segments. Relays are, however, components of 3-D segmented fault arrays and it is not clear the extent to which departures from parallel fault segments, such as those associated with 3-D bifurcating fault surfaces (Huggins et al., 1995; Walsh et al., 2003), will impact both the geometry and growth of relays. The models presented do not include layering, a feature that could exercise a significant control on the evolution and breaching of relays (Walsh et al., 1999). The presence of layering might be expected to

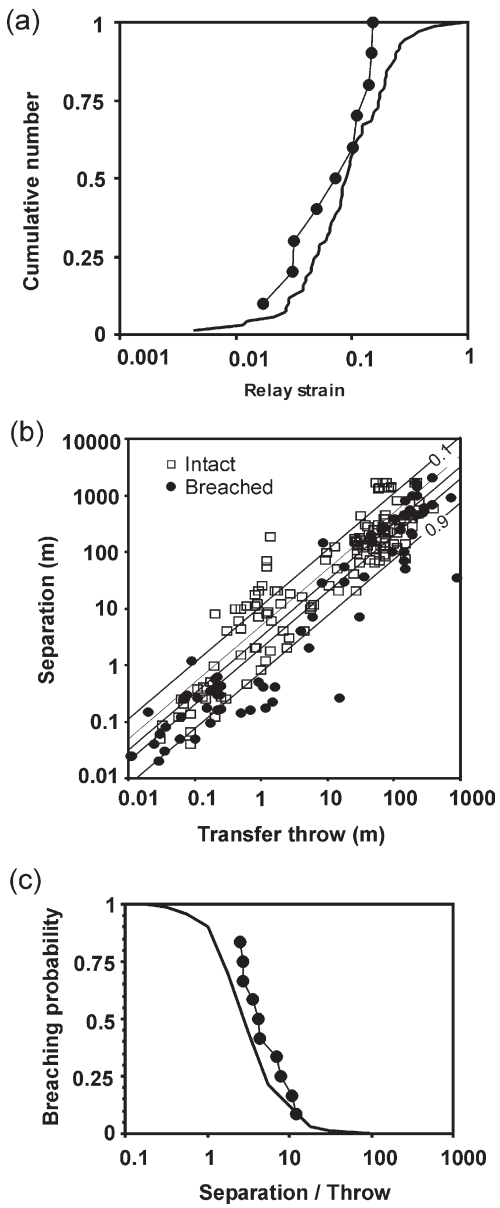

Fig. 11. (a) Normalized cumulative number of relay breaching strains for natural (solid line, $N = 70$) and model (dots, $N = 10$) relay zones. Each point in the model dataset represents one of three planes of inspection in a model (Fig. 8); breaching did not occur for two planes of inspection up to the maximum imposed relay strains of 0.2. (b) Plot of relay zone fault separation versus transfer throw for intact and breached relay zones. Lines are contours of probability (0.1, 0.3. 0.5, 0.7 and 0.9) of breaching. The data are from both published (Wessley, 1988; Childs et al., 1993, 1995; Peacock and Sanderson, 1994; Dawers and Anders, 1995; Cartwright et al., 1996; Huggins, 1996; Davies et al., 1997; Willemse, 1997; Foxford et al., 1998; Morley and Wonganan, 2000) and unpublished seismic and outcrop studies. (c) Curves of breaching probability for the natural and model datasets. The model derived curves in (a) and (c) are based on three Springwell Sandstone models and one Navajo sandstone model.

facilitate bed-parallel slip and associated ramp rotation, to provide higher relay strains at breaching; a perspective that is supported by our unpublished observational and modelling data. A further shortcoming of our models is that they do not incorporate the formation of relays, including the propagation and segmentation processes involved. Future work should attempt to reproduce the entire growth history of relays, examining the principal controls on their formation through to breaching and beyond.

7. Conclusions

1. Relay zone models based on bonded particle simulations using the distinct element method code PFC^{3D} successfully reproduce the geometries, displacement profiles and strains recorded in neutral (i.e. slip-parallel) relay zones on normal faults that cut homogeneous sandstone host rocks.
2. Relay zones are stable structures that 'grow' by progressive rotation of an approximately planar ramp with limited fault tip propagation.
3. Stable growth ends when a breaching fault propagates across the top or bottom of the relay ramp. Breaching fault propagation is not instantaneous and the relay ramp continues to rotate until the relay zone is hard linked in 3-D.
4. Breached relays that are hard linked in 3-D accommodate displacement on the through-going fault surface. The inactive relay ramp and associated splay fault are carried passively in the footwall/hanging wall of the through-going fault.
5. Distinct element models reproduce the essential features of established conceptual models for relay growth and breaching.

Acknowledgements

This work was funded through an Industry Technology Facilitator (ITF) Joint Industry Project sponsored by ExxonMobil, Norsk Hydro, JNOC and Statoil (1999–2001). We are very grateful to Jim Hazzard for providing his Springwell sandstone calibrations. Thanks to Phil Hall, Elizabeth Sweeney and Adriaan van Herk of the Fault Analysis Group for assistance with data analysis. Chris Dart, Hugh Kerr, Dave Reynolds, Martin Schöpfer, Bill Shea, Øyvind Steen, Uko Suzuki, Jon Vold and especially Peter Vrolijk are thanked for insightful discussion. We thank Juliet Crider and Nancye Dawers for providing constructive reviews, and David Ferrill for his editorial handling.

References

Antonellini, M.A., Pollard, D.D., 1995. Distinct element modelling of deformation bands in sandstones. Journal of Structural Geology 17, 1165–1182.

Cartwright, J.A., Trudgill, B.D., Mansfield, C.S., 1995. Fault growth by segment linkage: an explanation for scatter in maximum displacement and trace length data from the Canyonlands Grabens of SE Utah. Journal of Structural Geology 17, 1319–1326.

Cartwright, J.A., Mansfield, C., Trudgill, B., 1996. The growth of normal faults by segment linkage. In: Buchanan, P.G., Nieuwland, D.A. (Eds.), Modern Developments in Structural Interpretation, Validation and Modelling, Geological Society, London, Special Publication, 99., pp. 163–177.

Chadwick, R.A., 1986. Extension tectonics in the Wessex Basin, southern England. Journal of the Geological Society of London 143, 465–488.

Chapman, T.J., Meneilly, A.W., 1991. The displacement patterns associated with a reverse reactivated normal fault. In: Roberts, A.M., Yielding, G., Freeman, B. (Eds.), The Geometry of Normal Faults, Geological Society, London, Special Publication, 56., pp. 183–191.

Childs, C., Easton, S.J., Vendeville, B.C., Jackson, M.P.A., Lin, S.T., Walsh, J.J., Watterson, J., 1993. Kinematic analysis of faults in a physical model of growth above a viscous salt analogue. Tectonophysics 228, 313–329.

Childs, C., Watterson, J., Walsh, J.J., 1995. Fault overlap zones within developing normal fault systems. Journal of the Geological Society of London 152, 535–549.

Childs, C., Watterson, J., Walsh, J.J., 1996. A model for the structure and development of fault zones. Journal of the Geological Society of London 153, 337–340.

Clausen, O.R., Korstgård, J.A., 1994. Displacement geometries along graben bounding faults in the Horn Graben, offshore Denmark. First Break 12, 305–315.

Crider, J.G., 2001. Oblique slip and the geometry of normal-fault linkage: mechanics and a case study from the Basin and Range in Oregon. Journal of Structural Geology 23, 1997–2009.

Crider, J.G., Pollard, D.D., 1998. Fault linkage: three-dimensional mechanical interaction between echelon normal faults. Journal of Geophysical Research 103, 24373–24391.

Cundall, P.A., 1971. A computer model for simulating progressive large scale movements in blocky rock systems. Proceeding of the Symposium of the International Society of Rock Mechanics (Nancy, France, 1971), Vol. 1, Paper No. II-8.

Cundall, P.A., Strack, O.D.L., 1979. A discrete numerical model for granular assemblies. Géotechnique 29, 47–65.

Davies, R.K., Crawford, M., Dula, W.F. Jr, Cole, M.J., Dorn, G.A., 1997. Outcrop interpretation of seismic-scale normal faults in southern Oregon: description of structural styles and evaluation of subsurface interpretation methods. Leading Edge 8, 1135–1141.

Dawers, N.H., Anders, M.H., 1995. Displacement-length scaling and fault linkage. Journal of Structural Geology 17, 607–614.

Finch, E., Hardy, S., Gawthorpe, R., 2003. Discrete element modelling of contractional fault-propagation folding above rigid basement blocks. Journal of Structural Geology 25, 515–528.

Foxford, K.A., Walsh, J.J., Watterson, J., Garden, I.R., Guscott, S.C., Burley, S.D., 1998. Structure and content of the Moab Fault Zone, Utah, USA, and its implications for fault seal prediction. In: Jones, G., Fisher, Q.J., Knipe, R.J. (Eds.), Faulting, Fault Sealing and Fluid Flow in Hydrocarbon Reservoirs, Geological Society, London, Special Publication, 147., pp. 87–103.

Gawthorpe, R.L., Leeder, M.R., 2000. Tectono-sedimentary evolution of active extensional basin. Basin Research 12, 195–218.

Gibson, J.R., Walsh, J.J., Watterson, J., 1989. Modelling of bed contours and cross-sections adjacent to planar normal faults. Journal of Structural Geology 11, 317–328.

Hazzard, J.F., 1998. Numerical modelling of acoustic emissions and dynamic rock behaviour. Ph.D. thesis, Keele University, UK.

Hazzard, J.F., Young, R.P., Maxwell, S.C., 2000. Micromechanical modeling of cracking a failure in brittle rocks. Journal of Geophysical Research 105, 16683–16697.

Huggins, P., 1996. Relay zones in intra-continental normal faults: geometry, mechanics and kinematics. Unpublished PhD thesis, University of Liverpool.

Huggins, P., Watterson, J., Walsh, J.J., Childs, C., 1995. Relay zone geometry and displacement transfer between normal faults recorded in coal-mine plans. Journal of Structural Geology 17, 1741–1755.

Itasca Consulting Group, 1999a. PFC3D—Particle Flow Code in 3 Dimensions. User's Guide, Itasca Consulting Group, Inc, Minneapolis, Minnesota, USA.

Itasca Consulting Group, 1999b. PFC3D—Particle Flow Code in 3 Dimensions. Theory and Background, Itasca Consulting Group, Inc, Minneapolis, Minnesota, USA.

Itasca Consulting Group, 1999c. PFC3D—Particle Flow Code in 3 Dimensions. FISH in PFC^{3D}, Itasca Consulting Group, Inc, Minneapolis, Minnesota, USA.

Larsen, P.-H., 1988. Relay structures in a Lower Permian basement-involved extension system, East Greenland. Journal of Structural Geology 10, 3–8.

Mandl, G., 1987. Discontinuous fault zones. Journal of Structural Geology 9, 105–110.

Morgan, J.K., 1999. Numerical simulations of granular shear zones using the distinct element method 2. Effects of particle size distribution and interparticle friction on mechanical behavior. Journal of Geophysical Research 104, 2721–2732.

Morgan, J.K., Boettcher, M.S., 1999. Numerical simulations of granular shear zones using the distinct element method 1. Shear zone kinematics and the micromechanics of localization. Journal of Geophysical Research 104, 2703–2719.

Morley, C.K., Wonganan, N., 2000. Normal fault displacement characteristics, with particular reference to synthetic transfer zones, Mae Moh Mine, Northern Thailand. Basin Research 12, 1–22.

Morley, C.K., Nelson, R.A., Patton, T.L., Munn, S.G., 1990. Transfer zones in the East African Rift system and their relevance to hydrocarbon exploration in rifts. AAPG Bulletin 74, 1234–1253.

Nicol, A., Watterson, J., Walsh, J.J., Childs, C., 1996. The shapes, major axis orientations and displacement patterns of fault surfaces. Journal of Structural Geology 18, 235–248.

Peacock, D.C.P., 2001. The temporal relationship between joints and faults. Journal of Structural Geology 23, 329–341.

Peacock, D.C.P., 2002. Propagation, interaction and linkage in normal fault systems. Earth-Science Reviews 58, 121–142.

Peacock, D.C.P., Sanderson, D.J., 1991. Displacements, segment linkage and relay ramps in normal fault zones. Journal of Structural Geology 13, 721–733.

Peacock, D.C.P., Sanderson, D.J., 1992. Effects of layering and anisotropy on fault geometry. Journal of the Geological Society, London 149, 793–802.

Peacock, D.C.P., Sanderson, D.J., 1994. Geometry and development of relay ramps in normal fault systems. AAPG Bulletin 78, 147–165.

Peacock, D.C.P., Zhang, X., 1994. Field examples and numerical modelling of oversteps and bends along normal faults in cross-section. Tectonophysics 234, 147–167.

Petersen, K., Clausen, O.R., Korstgård, J.A., 1992. Evolution of a salt-related listric growth fault near the D-1 well, block 5605, Danish North Sea: displacement history and salt kinematics. Journal of Structural Geology 14, 565–577.

Ramsay, J.G., Huber, M.I., 1987. The Techniques of Modern Structural Geology, Volume 2: Folds and Fractures, Academic Press, London.

Stein, R.S., Barrientos, S.E., 1985. Planar high-angle faulting in the Basin and Range: geodetic analysis of the 1983 Borah Peak, Idaho, earthquake. Journal of Geophysical Research 90, 11355–11366.

Stewart, I.S., Hancock, P.L., 1991. Scales of structural heterogeneity within neotectonic normal fault zones in the Aegean region. Journal of Structural Geology 13, 191–204.

Strayer, L.M., Suppe, J., 2002. Out-of-plane motion of a thrust sheet during along-strike propagation of a thrust ramp: a distinct element approach. Journal of Structural Geology 24, 637–650.

Thomas, A.L., 1993. Poly3d: a three-dimensional, polygonal element, displacement discontinuity boundary element computer program with applications to fractures, faults and cavities in the Earth's crust. M.S. thesis, Stanford University, California.

Trudgill, B.D., Cartwright, J.A., 1994. Relay ramp forms and normal fault

linkages-Canyonlands National Park, Utah. Geological Society of America Bulletin 106, 1143–1157.

Walsh, J.J., Watterson, J., 1990. New methods of fault projection for coal mine planning. Proceedings of the Yorkshire Geological Society 48, 209–219.

Walsh, J.J., Watterson, J., 1991. Geometric and kinematic coherence and scale effects in normal fault systems. In: Roberts, A.M., Yielding, G., Freeman, B. (Eds.), The Geometry of Normal Faults, Geological Society, London, Special Publication, 56., pp. 193–203.

Walsh, J.J., Watterson, J., Bailey, W.R., Childs, C., 1999. Fault relays, bends and branch-lines. Journal of Structural Geology 21, 1019–1026.

Walsh, J.J., Childs, C., Meyer, V., Manzocchi, T., Imber, J., Nicol, A., Tuckwell, G., Bailey, W.R., Bonson, C.G., Nell, P.A.R., Strand, 2001. Geometrical controls on the evolution of normal fault systems. In: Holdsworth, R.E., Strachan, R.A., Magloughlin, J.F., Knipe, R.J. (Eds.), The Nature and Tectonic Significance of Fault Zone Weakening, Geological Society, London, Special Publication, 186., pp. 157–170.

Walsh, J.J., Bailey, W.R., Childs, C., Nicol, A., Bonson, C.G., 2003. Formation of segmented normal fault: a 3-D perspective. Journal of Structural Geology 25, 1251–1262.

Wessley, G., 1988. Structure and development of the Vienna Basin in Austria. In: Royden, L.H., Horváth, F. (Eds.), The Pannonian Basin—A Study in Basin Evolution, AAPG Memoir, 45., pp. 333–346.

Willemse, E.J.M., 1997. Segmented normal faults: correspondence between three-dimensional mechanical models and field data. Journal of Geophysical Research 102, 675–692.

Willemse, E.J.M., Pollard, D.D., Aydin, A., 1996. Three-dimensional analyses of slip distributions on normal fault arrays with consequences for fault scaling. Journal of Structural Geology 18, 295–309.

Wu, B., King, M.S., Hudson, J.A., 1991. Stress-induced ultrasonic wave velocity anisotropy in a sandstone. International Journal of Rock Mechanics, Mining Sciences and Geomechanical Abstracts 28, 101–107.